A Novel Six-Axis Force/Torque Sensor for Robotic Applications

Uikyum Kim, Dong-Hyuk Lee, Yong Bum Kim, Dong-Yeop Seok, and Hyouk Ryeol Choi, *Member, IEEE*

Abstract—**This paper presents a novel six-axis force/ torque (F/T) sensor for robotic applications that is self-contained, rugged, and inexpensive. Six capacitive sensor cells are adopted to detect three normal and three shear forces. Six sensor cell readings are converted to F/T information via calibrations and transformation. To simplify the manufacturing processes, a sensor design with parallel and orthogonal arrangements of sensing cells is proposed, which achieves the large improvement of the sensitivity. Also, the signal processing is realized with a single printed circuit board and a ground plate, and thus, we make it possible to build a lightweight six-axis F/T sensor with simple manufacturing processes at extremely low cost. The sensor is manufactured and its performances are validated by comparing them with a commercial six-axis F/T sensor.**

Index Terms—**Capacitive sensor, low cost, simple manufacturing, six-axis force/torque (F/T) sensor.**

I. INTRODUCTION

OBTAINING force information is essential in extensive robotics research and applications [1]–[4]. A six-axis force/torque (F/T) sensor measures all the force and torque components at a certain point on a plane, that is, three orthogonal forces (F_X, F_Y, and F_Z), and three orthogonal torques (T_X, T_Y, and T_Z) [5]. Therefore, the F/T sensor is important in providing high-quality services in various robotic applications such as manipulation, humanoid, surgical robot, telemanipulation, and so on [6]–[9]. Also, it makes delicate tasks possible that are rather impossible for industrial robots such as polishing, part insertion, and cooperative manipulation with humans [10].

Although the F/T sensor is prerequisite in advanced services, it has not been extensively used in real applications. The primary reason is it is fragile and too much expensive. It is due to complex manufacturing and difficult assembly processes by using strain

gauges as their core sensing method [9], [11], [12]. Rugged and inexpensive six-axis F/T sensors are desirable.

Meanwhile, capacitive-type sensors have been considered as alternatives, because it is simple in its structure without additional transducers like strain gauges [2], [4]. Moreover, they can operate with high sensitivity and detect extremely small displacements with low influence of temperature changes [2]. Up to now many capacitive-type, multiaxis force sensors have been developed. Some of them are only able to provide three-axis force information [13], [14]. Kim *et al.* developed a capacitive-type six-axis F/T sensor [15], but the sensor is made by bonding electrodes onto a complex structure, and thus, it suffers from the problem similar to the resistive-type sensors. Also, Lee *et al.* designed a capacitive-type six-axis sensor with a simple configuration [16]. However, low stiffness and complexity of the three-dimensional printed elastic structure are drawbacks hampering its practical applications.

First, this paper proposes a new capacitive force sensing method. The method detects the capacitance change between two orthogonal electrodes, and thus, it is highly sensitive because the fringe effect is dominantly used. It has nonlinear characteristics, but it is successfully compensated by using the calibration technique developed in this study. Also, a novel six-axis F/T sensor is proposed, which detects six force elements by using proposed six capacitance sensing cells. Three normal and three shear forces are read, from which six force and torque values are derived. The proposed method makes it possible to produce a six-axis F/T sensor with simple manufacturing procedures. In this design, the sensing range and sensitivity of the sensor can be easily adjusted by changing only a deformable part, and thus, it is easily customizable. As an example, we apply the proposed method on manufacturing a miniature six-axis F/T sensor with a diameter of 25 mm and a height of 19 mm, but the method is not limited to this. In this design, all the signal processing electronics are integrated into the inner part of the sensor, but its weight does not exceed 15 g. Therefore, the sensor is useful in many robotic applications.

II. DESIGN OF SIX-AXIS F/T SENSOR

A. Principles of Capacitive Sensing

As shown in Fig. 1(a), a six-axis F/T sensor measures three directional forces (F_X, F_Y, and F_Z) and three directional torques (T_X, T_Y, and T_Z) at a point of the sensor's surface. To measure the forces and torques, force information along at least six
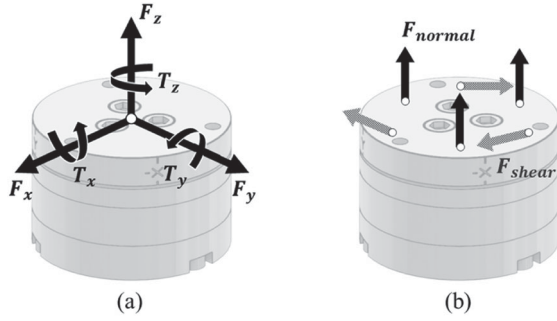
Fig. 1. Schematics for a six-axis F/T element and the forces needed to obtain it. (a) Six-axis F/T directions at a material point on a sensor. (b) Three normal and three shear forces at different places or directions.
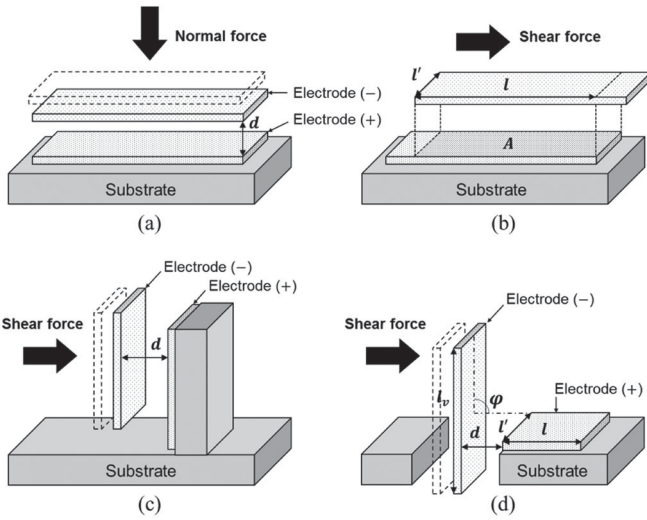

Fig. 2. Capacitance sensing principles. (a) Motion of a negative electrode by an applied normal force. (b) Motion of a negative electrode by an applied shear force. (c) Using two parallel electrode plates. (d) Using two orthogonal electrode plates.

different directions or locations is needed [17]. Fig. 1(b) displays the force sensing elements designed to measure the forces. On the sensor's surface, two kinds of force sensing are performed, that is, normal force sensing and shear force one. The sensing points are symmetrically placed at even intervals circumferentially [17]. The obtained three normal and three shear forces make it possible to extract six-axis F/T values by using the geometric relationship.

Typically, a capacitive sensor consists of two conductive electrodes and dielectric material sandwiched between them. The relative positioning between two conductive electrodes is sensed by measuring the capacitance [4], [16]. As illustrated in Fig. 2(a) and (b), the sensing method can measure both normal and shear forces. In the case that a normal force is applied, capacitance varies due to the variation in distance d produced by the force applied on the upper electrode plate, as represented in Fig. 2(a). Fig. 2(b) shows that shear forces applied to the plate change the size of the overlapping area A, and thus, the capacitance does. The length l of the area of the sensor usually is designed to be

much longer than the distance d to minimize the fringing effect. Therefore, the resulting capacitance variation can be expressed as [4]

$$\Delta C = C_{\text{init}} - C_\Delta = \varepsilon_0 \varepsilon_r \left(\frac{\Delta A}{\Delta d} \right) \quad (1)$$

where C_{init} is the initial capacitance, and C_Δ denotes the final capacitance. ε_0 and ε_r represent the dielectric constant and static relative permittivity, respectively. Assuming that $l/d = 10$ for a film-type sensor, C_{init} can be calculated by

$$C_{\text{init}} = \varepsilon_0 \varepsilon_r 10 l' \quad (2)$$

where l' is the width of the area. The capacitance change depending on that of distance is given by

$$\Delta C_d = C_{\text{init}} - C_d = \varepsilon_0 \varepsilon_r \left(\frac{\Delta d}{d'} \right) l' \quad (3)$$

$$d' = d_0 - \Delta d \quad (4)$$

where ΔC_d is the capacitance change due to that of the distance. d_0 represents the initial distance and Δd means the distance change. As shown in Fig. 2(b), assuming that the change in the length of the overlapping area equals to that of the distance, the capacitance change is calculated as follows:

$$\Delta C_A = C_{\text{init}} - C_A = \varepsilon_0 \varepsilon_r \left(\frac{\Delta d}{d' + \Delta d} \right) l' \quad (5)$$

where ΔC_A is the capacitance variation due to the change in area. Assuming that the external normal and shear forces are of the same magnitude, changes of capacitance for the same distance change, for example $\Delta d = 0.1 d_0$, can be rewritten by

$$\Delta C_d = \varepsilon_0 \varepsilon_r 1.1 l'$$
$$\Delta C_A = \varepsilon_0 \varepsilon_r 0.1 l' \quad (6)$$

respectively. Consequently, the method of shear force sensing by using changes in the plate's overlapping area is even less sensitive, that is, less than 1/10 of the normal force sensing method.

On the contrary, as shown in Fig. 2(c) and (d), shear force sensing can be done by using the distance change along the the shear force's direction. As shown in Fig. 2(c), shear forces can be detected by the change in distance between a vertical ground electrode and a parallel positive electrode. However, the manufacturing process becomes complicated because extra parts are needed for supporting the electrode vertically.

As another way of electrode layout, an orthogonal configuration between two electrodes as shown in Fig. 2(d) can be considered. In this configuration, the capacitance between two orthogonal electrodes changes largely depending on the relative distance, and it is the case that the fringing effect is actively used. Thus, the sensitivity is greatly improved while manufacturing processes are kept simple. For example, when the angle ψ between two electrodes is 90° and the electrode is placed at the center of the ground's surface, the capacitance variation
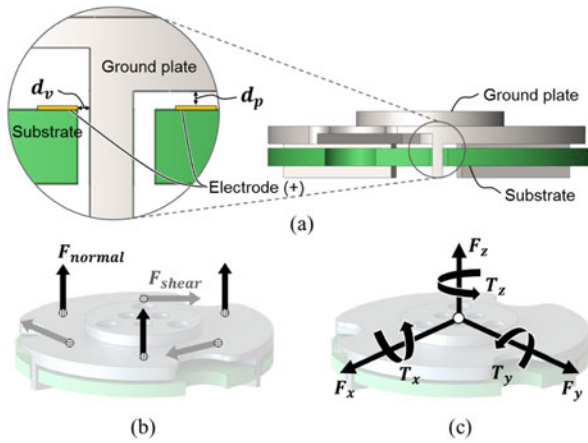
Fig. 3. Configuration of sensing elements with the proposed sensing methods. (a) Locations of two sensing cells for measuring normal and shear forces. (b) Arrangement of the three normal and three shear forces measured by the six capacitance sensing cells. (c) Six-axis F/T at the central material point.

between two electrodes can be derived as follows [18], [19]:

$$
\begin{aligned}
\Delta C_{d_v} &= C_{\text{init}_v} - C_{d_v} \\
&= 2\varepsilon_0\varepsilon_r \left[\left(\frac{K'(k_{\text{in}}(d_0))}{K(k_{\text{in}}(d_0))} + \frac{K'(k_{\text{out}}(d_0))}{K(k_{\text{out}}(d_0))} \right) \right. \\
&\quad \left. - \left(\frac{K'(k_{\text{in}}(d'))}{K(k_{\text{in}}(d'))} + \frac{K'(k_{\text{out}}(d'))}{K(k_{\text{out}}(d'))} \right) \right]
\end{aligned}
\tag{7}
$$

where C_{init_v} is the initial capacitance between two orthogonal electrodes and ΔC_{d_v} is the variation in capacitance due to distance variation, respectively. $K(k)$ represents the complete elliptic integral of the first kind [18]. k_{in} and k_{out} are the modulus, expressed as functions of distance d, and include the structural information [19]:

$$
k_{\text{in}}(d) = \frac{d}{d+l} \sqrt{\frac{(d+l)^2 + (0.5l_v)^2}{d^2 + (0.5l_v)^2}}
$$

$$
k_{\text{out}}(d) = \sqrt{\frac{d^{(2/3)}((d+l)^{(2/3)} + (0.5l_v)^{(2/3)})}{(d+l)^{(2/3)}(d^{(2/3)} + (0.5l_v)^{(2/3)})}}
\tag{8}
$$

where l_v is the length of the vertical ground. From (7) and (8) with $\Delta d = 0.1d_0$, the capacitance variation can be obtained as follows:

$$
\Delta C_{d_v} = \varepsilon_0 \varepsilon_r 0.47 l'.
\tag{9}
$$

Comparing with (6), it is noted that the sensitivity of shear force sensing becomes five times higher than that of using two parallel plates. In this work, we apply two parallel-electrode configurations for sensing normal forces, and two orthogonal-electrode configurations are used for sensing shear forces.

B. Design of Sensing Cells

Fig. 3 explains the electrode's arrangement for the capacitance sensing cells to obtain the six-axis F/T value. As shown

in Fig. 3(a), a structured plate is inserted into the empty places of a substrate to be used as the ground electrode, and positive electrodes are placed on the substrate. Two gaps between the ground plate and the substrate in the left inset of Fig. 3(a) are the distance d_p between two parallel plates, and the distance d_v between two orthogonal plates, respectively. As explained, the normal displacement is measured by sensing the change of capacitance between the parallel positive electrode and the ground one, whereas the shear displacement is obtained by sensing the capacitance change between the ground plate and the orthogonal positive electrode.

The positive electrode of the parallel sensing cell should be located sufficiently far from the vertical surface of the ground plate to guarantee that the capacitance of this cell is unaffected by shear displacements. Also, the positive electrode for shear force sensing should be located sufficiently far from the parallel face of the ground electrode to guarantee that the capacitance of its sensing cell stays unaffected by normal displacements. As shown in Fig. 3(b) and (c), two kinds of gaps are placed on six regions at even intervals circumferentially. Thus, sensor readings provide information that can be transformed into a six-axis F/T value [4], [17]. In this configuration, the substrate and positive electrodes can be implemented by using single printed circuit board (PCB), and thus, six-axis F/T sensing can be realized just with assembling two plates.

C. Design of Six-Axis F/T Sensor

Fig. 4(a) shows the exploded view of the proposed sensor. It is composed of five mechanical parts and two PCBs. The five parts are: top plate, deformable plate, ground plate, case part, and bottom plate. One of two PCBs measures capacitance values and the other one processes the capacitance data and send them out as digital data.

When external forces or torques are applied to the surface of the top plate, the internal structure of the deformable plate deforms. The internal structure consists of three sets of cross elastic and compliant beams, which act as flexure hinges to generate displacements in response to external forces or torques. The ground plate, suspended from the deformable plate, makes six air gaps between its surfaces and six electrodes of an electrode PCB. The ground plate moves according to the movement of the deformable plate. The electrode PCB and signal processing PCB are fixed in the case part. The outer wiring connected to the signal processing circuit is fixed onto the bottom plate.

In the proposed design, there are only three areas with bolted connections, that is, between the top and deformable plates, the deformable and ground plates, and the deformable and bottom plates. Through these connections, the common ground of the signal processing circuit has electrical connections to all the plates to shield outer electromagnetic interferences [4]. The proposed design is the advantage of compact composition and miniaturization with all the signal processing units integrated. Thus, it allows much simpler manufacturing processes, and guarantees cost-effective mass production.
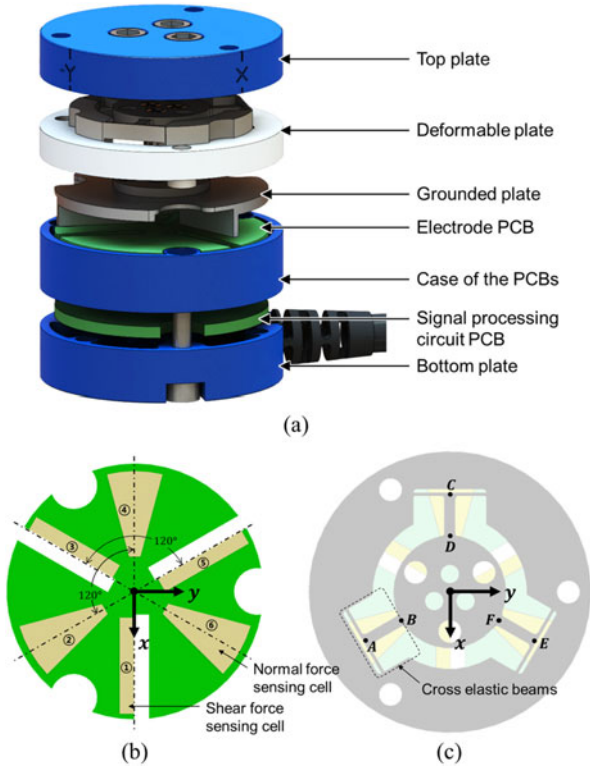
Fig. 4. (a) Exploded view of all the assembly parts of the proposed sensor. (b) Composition of an electrode PCB. (c) Composition of a deformable plate.
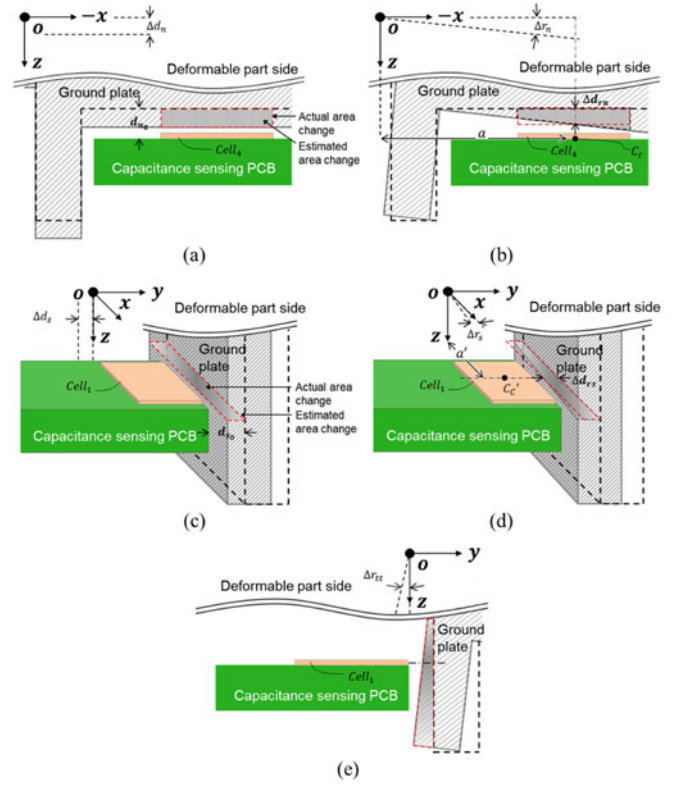

Fig. 5. Situations where capacitance variations are measured by a normal force sensing cell and a shear force sensing cell. (a) Displacement by applied normal force (F_Z). (b) Displacement by applied torque (T_Y). (c) Displacement by applied shear force (F_Y). (d) Displacement by applied torque (T_Z). (e) Displacement by applied torque (T_Y).

III. STRUCTURAL ANALYSIS AND SIMULATIONS

A. Displacement and Capacitance Variation Analysis

To know the relationship between the applied F/T and the capacitance variation, it is necessary to conduct structural analysis. Fig. 4(b) and (c) show the labeled composition of the electrode PCB and the deformable plate. As shown in Fig. 4(b), there are six capacitance sensing cells on the PCB, that is three normal force sensing cells ($Cell_2$, $Cell_4$, and $Cell_6$) and three shear force sensing cells ($Cell_1$, $Cell_3$, and $Cell_5$). They are symmetrically placed at regular intervals as shown in Fig. 4(c).

As explained, the three normal and three shear forces can be transformed into a six-axis F/T from the geometrical relation. In other words, from the three normal forces we can extract F_Z, T_X, and T_Y, and from the shear forces we can extract F_X, F_Y, and T_Z. The relationship can be expressed as [20]

$$\mathbf{T_N} \cdot [F_{N1}\ F_{N2}\ F_{N3}]^T = [F_Z\ T_X\ T_Y]^T$$

$$\mathbf{T_S} \cdot [F_{S1}\ F_{S2}\ F_{S3}]^T = [F_X\ F_Y\ T_Z]^T \qquad (10)$$

where $[F_{N1}\ F_{N2}\ F_{N3}]^T$ is the vector of normal forces, and $[F_{S1}\ F_{S2}\ F_{S3}]^T$ denotes the vector of shear forces. $\mathbf{T_N}$ and $\mathbf{T_S}$ are 3×3 transformation matrices.

Fig. 5(a) and (b) illustrate how the normal force sensing cells detects capacitance variations. The normal force sensing cell labeled as 4 ($Cell_4$) is analyzed due to its orthogonal placement within the sensor coordinate system. As shown in Fig. 5(a), when the deformable plate is displaced (Δd_n) by the normal

force, a capacitance variation is measured by the sensing cell as per (1). The capacitance of the cell is also changed when the angular displacement Δr_n occurs by the applied torque (T_Y). As shown in Fig. 5(b), the shape of the actual displacement is a trapezoid, which can be approximated as a rectangle [21]. In other words, depending on the distance a between z axis and the sensing center C_c of the cell, the angle displacement and the torque can be treated as a displacement Δd_{rn} along the z direction generated by the normal force. Because the angular displacement by T_X offsets the area change, the capacitance is not changed [16]. To eliminate the influence of the shear force, the normal force sensing cell is designed to be smaller than the ground plate surface [4]. Therefore, the capacitance variation ΔC_N of the cell is calculated by using (1) with d' defined such as

$$d' = d_{n_0} - (\Delta d_n + \Delta d_{rn}) \qquad (11)$$

where d_{n_0} is the initial distance between the cell and the ground surface.

Fig. 5(c) and (d) show the case that the shear force sensing cells detects capacitance variations. The shear force sensing cell labeled as 1 ($Cell_1$) is analyzed similarly to the normal force sensing cell $Cell_4$. As illustrated in Fig. 5(c), when the shear force makes the displacement Δd_s, the sensing cell measures the capacitance variation according to (7) and (8). The capacitance is also changed in the case of the angular displacement under T_Z due to the trapezoidal change in the area as shown in

Fig. 5(d). The trapezoidal shape can be approximated by a rectangle. Thus, the angle displacement and moment can be treated as a displacement Δd_{rs} along the y direction and a shear force according to the distance a' between z axis and the sensing center $C_{c'}$ of the cell similarly. Because the cell is smaller than the ground surface, the displacement created by F_X does not have influence on the capacitance. As the result, the capacitance change ΔC_S can be calculated by (7) and (8) with d' such as

$$d' = d_{s_0} - (\Delta d_s + \Delta d_{rs}) \tag{12}$$

where d_{s_0} is the initial distance between the cell and the grounded surface. Through the analysis, it is noted that the normal and shear force sensing cells are influenced by normal and shear forces, respectively. However, in actual experiments the cell is also influenced by T_X and T_Y as shown in Fig. 5(e). For this reason, the influence needs to be eliminated with the scaled T_X and T_Y measured by the three normal force sensing cells during an automated F/T calibration process using an experimental setup.

B. Applied F/T and Displacement Analysis

To derive the relation between capacitances at two types of cell and the normal and shear forces, the displacements of the deformable plate are analyzed under two forces (F_Y and F_Z) and two torques (T_Y and T_Z). The effect of F_X is symmetrical to that of F_Y and the effect of T_X is symmetrical to that of T_Y. Fig. 6(a) shows the detailed structure of the deformable plate. The flexure of the plate is supported by three cross elastic and compliant beams, whose geometry is represented with only six parameters such as l_1, l_2, b_1, b_2, h_1, and h_2 [22]. Therefore, it is easy to change the relation between displacements and the applied forces. In other words, the range and resolution of the proposed sensor can be easily changed by the design of the flexure hinges.

In this study, we conduct the structural analysis according to [23]. The cross elastic beams and compliant beams are considered to be the only deformable components and all the other parts of the plate are considered rigid bodies. The deflection characteristics of the beams under forces and torques (F_Y, F_Z, T_Y, and T_Z) are analyzed based on Timoshenko beam theory [23]. The deformation of the flexure caused by the normal force (F_Z) is presented in Fig. 6(b). In this case, all the beams are deformed. The cross elastic beams are considered as propped-cantilever beams, and the compliant beams are considered fixed beams. Given the symmetry of the structure, the analysis is made only for deformation points E and F. $\Delta d_{F_{Fz}}$, the vertical displacement at F can be expressed as

$$\Delta d_{F_{Fz}} = \left(\frac{l_1^3}{3D_1} + \frac{l_1}{C_1} \right) F_{F_{Fz}} \tag{13}$$

where $D_1 = EI_1$, $C_1 = kGA_1$, $I_1 = \frac{b_1 h_1^3}{12}$, $A_1 = b_1 h_1$. $F_{F_{Fz}}$ is the normal force at beam FE. The displacement at E, $\Delta d_{E_{Fz}}$ is calculated similarly as follows:

$$\Delta d_{E_{Fz}} = \left(\frac{l_2^3}{12D_{21}} + \frac{l_2}{C_2} \right) F_{E_{Fz}} \tag{14}$$
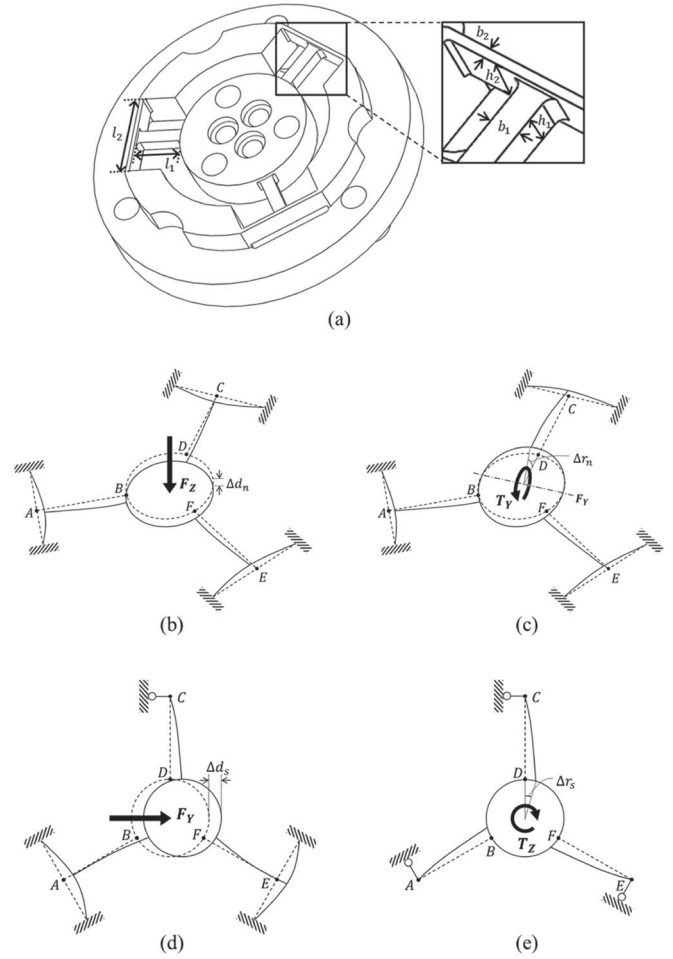

Fig. 6. Design and mechanical models of the deformable plate. (a) Deformable plate composed of three cross elastic beams and three compliant beams. (b) F_Z. (c) T_Y. (d) F_Y. (e) T_Z.

where $D_{21} = EI_{21}$, $C_2 = kGA_2$, $I_{21} = \frac{h_2 b_2^3}{12}$, $A_2 = b_2 h_2$. $F_{E_{Fz}}$ represents the normal force at the compliant beam at E. Therefore, the deformation (Δd_n) under F_Z can be written as

$$\Delta d_n = \Delta d_{F_{Fz}} + \Delta d_{E_{Fz}}. \tag{15}$$

Also, according to the force equilibrium of the flexure, F_Z leads to

$$F_Z = 3F_{F_{Fz}} = 6F_{E_{Fz}}. \tag{16}$$

Thus, Δd_n is calculated based on (13) to (16) as

$$\Delta d_n = \frac{1}{3} (a_1 + a_2) F_Z \tag{17}$$

where $a_1 = \left(\frac{l_1^3}{3D_1} + \frac{l_1}{C_1} \right)$, $a_2 = \left(\frac{l_2^3}{24D_{21}} + \frac{l_2}{2C_2} \right)$.

The angular deformation of the flexure under T_Y is shown in Fig. 6(c). Here, the deformation at points D and C is upward, and the deformation at points A, B, E, and F is downward. The angular deformations under T_Y of the DC and FE beams along the F_Y axis also represent an angle displacement (Δr_n).

Therefore, the angular displacement can be calculated as

$$\Delta r_n = \left(a_1 F_{F_{\mathrm{T_y}}} + 2a_2 F_{E_{\mathrm{T_y}}}\right)\frac{1}{(l_1+r)\cos(\pi/3)}$$

$$= \frac{C_1 F_{D_{\mathrm{T_y}}} l_1^3 + 3D_1 F_{D_{\mathrm{T_y}}} l_1 + 3C_1 D_1 \Delta d_{C_{\mathrm{T_y}}}}{3C_1 D_1 (l_1+r)} \quad (18)$$

where $F_{E_{\mathrm{T_y}}} = 0.5F_{F_{\mathrm{T_y}}}$, $\Delta d_{C_{\mathrm{T_y}}} = F_{D_{\mathrm{T_y}}} a_2$, and $F_{E_{\mathrm{T_y}}}$ and $F_{F_{\mathrm{T_y}}}$ are the normal forces on the beam FE and on the compliant beam at E. $F_{D_{\mathrm{T_y}}}$ represents the normal force on beam DC. F/T equations of equilibrium of the flexure lead to

$$T_Y = T_{D_{\mathrm{T_y}}} - F_{D_{\mathrm{T_y}}} r + 2\left(T_{F_{\mathrm{T_y}}}\cos(\pi/3) - F_{F_{\mathrm{T_y}}} r\right) \quad (19)$$

where $T_{D_{\mathrm{T_y}}} = F_{D_{\mathrm{T_y}}} l_1$, $T_{F_{\mathrm{T_y}}} = F_{F_{\mathrm{T_y}}} l_1$, and, r is the radius of the circle. (19) can be rewritten as

$$F_{D_{\mathrm{T_y}}} = W_T T_Y \quad (20)$$

where $W_T = \frac{1}{(3l_1 - r(1 + \frac{2}{\cos(\pi/3)}))}$. Using (18), Δr_n is calculated as

$$\Delta r_n = \frac{C_1 l_1^3 + 3D_1 l_1 + a_2}{3C_1 D_1 (l_1+r)} W_T T_Y. \quad (21)$$

Fig. 6(d) shows the deformation of the flexure under F_Y. In this case, the cross elastic beams BA and FE are simplified as a propped-cantilever beam, and the compliant beams at points A and E are as cantilever beams. The compliant beam at C is simplified as a roller support. The displacements at F and E can then be summarized as

$$\Delta d_{F_{\mathrm{F_y}}} = a_1 F_{F_{\mathrm{F_y}}} \cos^2(\pi/3)$$

and

$$\Delta d_{E_{\mathrm{F_y}}} = \left(\frac{l_2^3}{12D_{22}} + \frac{l_2}{C_2}\right) F_{E_{\mathrm{F_y}}}\cos^2(\pi/6) \quad (22)$$

where $D_{22} = EI_{22}$, $I_{22} = \frac{h_2 b_2^3}{12}$, and $F_{F_{\mathrm{F_y}}}$ and $F_{E_{\mathrm{F_y}}}$ are the shear forces on the cross beam EF and on the compliant beam at E, respectively. The displacement at point D can be written as

$$\Delta d_{D_{\mathrm{F_y}}} = a_1 F_{D_{\mathrm{F_y}}} \quad (23)$$

where $F_{D_{\mathrm{F_y}}}$ is the shear force on cross beam CD. The movement of the flexure at point D and F along the F_Y axis is the displacement (Δd_s) under F_Y. Therefore, Δd_s is expressed as

$$\Delta d_s = \Delta d_{F_{\mathrm{F_y}}} + \Delta d_{E_{\mathrm{F_y}}} = \Delta d_{D_{\mathrm{F_y}}}. \quad (24)$$

Accordingly, based on the force equilibrium of the flexure, considering F_Y leads to

$$F_Y = F_{D_{\mathrm{F_y}}} + 2F_{F_{\mathrm{F_y}}} + 4F_{E_{\mathrm{F_y}}} \quad (25)$$

where $F_{E_{\mathrm{F_y}}} = 0.5F_{F_{\mathrm{F_y}}}$. (25) can be rewritten according to (22) and (23) such as

$$F_{D_{\mathrm{F_y}}} = W_F F_Y \quad (26)$$

where $W_F = \frac{a\cos^2(\pi/3) + c\cos^2(\pi/6)}{a\cos^2(\pi/3) + c\cos^2(\pi/6) + 4a}$. Δd_s is calculated as

$$\Delta d_s = a_1 W_F F_Y. \quad (27)$$

In the case of T_Z, all cross elastic beams have equal bending motions. These beams are simplified as propped-cantilever beams, and the compliant beams are idealized as elastic supports of beams BA, DC, and FE as shown in Fig. 6(e). The displacement at $\Delta d_{F_{\mathrm{T_z}}}$ is given by

$$\Delta d_{F_{\mathrm{T_z}}} = a_1 F_{F_{\mathrm{T_z}}} \quad (28)$$

where $F_{F_{\mathrm{T_z}}}$ represents the shear force on the elastic beam EF. In this situation, based on the F/T equilibrium of the flexure, T_Z can be expressed as

$$T_Z = 3F_{F_{\mathrm{T_z}}} r + 3T_{F_{\mathrm{T_z}}} = 3(r+l_1)F_{F_{\mathrm{T_z}}} \quad (29)$$

where $T_{F_{\mathrm{T_z}}}$ is the bending moment of the beam FE's front surface, and $T_{F_{\mathrm{T_z}}} = F_{F_{\mathrm{T_z}}} l_1$. The angle displacement (Δr_s) is given by

$$\Delta r_s = \frac{1}{r+l_1}\Delta d_{F_{\mathrm{T_z}}}. \quad (30)$$

Using (28) and (29), the displacement can be represented as a function of T_Z as follows:

$$\Delta r_s = \frac{l_1^3 C_1 + 3D_1 l_1}{9C_1 D_1 (r+l_1)^2} T_Z. \quad (31)$$

Consequently, because $F_Z = F_N$, $T_Y = F_n a$, $F_Y = F_S$, and $T_Z = F_S a'$, (11) and (12) can be written as

$$d' = d_{n_0} - \left[\frac{1}{3}(a_1+a_2) + \frac{C_1 l_1^3 + 3D_1 l_1 + a_2}{3C_1 D_1 (l_1+r)} W_T a\right]F_N \quad (32)$$

and

$$d' = d_{s_0} - \left(a_1 W_F + \frac{l_1^3 C_1 + 3D_1 l_1}{9C_1 D_1 (r+l_1)^2} a'\right)F_S \quad (33)$$

respectively. Thus, the relation between the normal force and capacitance variation at the normal force sensing cell is calculated by using (1) and (32). The relation between the shear force and capacitance variation at the shear force sensing cell is calculated using (7), (8), and (33).

C. Six-axis F/T Transformation Using Three Normal and Three Shear Forces

By using the geometrical relations between the directions and points of application of the forces and the six-axis F/T, the six-axis F/T transformation is derived. According to (10), the three shear forces can be used to obtain F_X, F_Y, and T_Z. As depicted in Fig. 7(a) F_X, F_Y, and T_Z are be expressed as

$$F_X = -F_{S2}\sin(\pi/3) + F_{S3}\sin(\pi/3)$$
$$F_Y = -F_{S1} + F_{S2}\sin(\pi/3) + F_{S3}\cos(\pi/3)$$
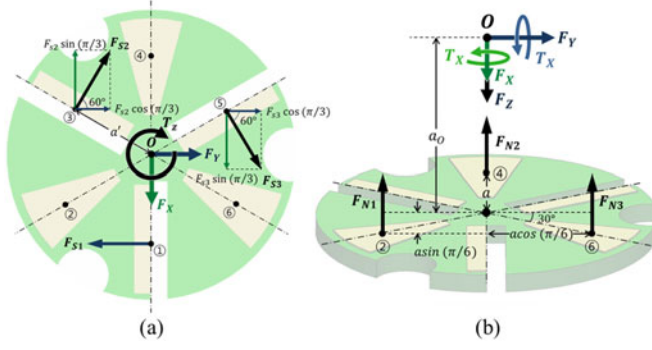$$T_Z = (F_{S1} + F_{S2} + F_{S3})a'/3. \quad (34)$$

Fig. 7. Normal and shear force analysis based on geometric relationship with the six-axis F/T. (a) Analysis of shear forces. (b) Analysis of normal forces.

As shown in Fig. 7(b), the three normal forces can be transformed into F_Z, T_X, and T_Y similarly.

$$F_Z = (F_{N1} + F_{N2} + F_{N3})/3$$
$$T_X = -F_{N1}a\cos(\pi/3) + F_{N2}a\cos(\pi/3)$$
$$T_Y = -F_{N1}a\sin(\pi/3) - F_{N2}a\sin(\pi/3) + F_{N3}a. \quad (35)$$

D. Simulations

Based on the theoretical analyses the behavior of the proposed sensor was simulated and the allowable F/T ranges were computed by using finite element analyses technique. The deformation under F_Y is similar to the one under F_X, and the deformation under T_Y is similar to the one under T_X. Therefore, only the four cases (F_Y, F_Z, T_Y, and T_Z) of flexure are analyzed. The parameters l_1, l_2, b_1, h_1, b_2, and h_2 are set, respectively. The flexure is made of aluminum 7075 with a modulus of elasticity of 71.7 GPa and tensile yield strength of 503 MPa. When the F/T-induced stress applied to the flexure goes over the yield strength, plastic deformation occurs. Accordingly, the allowable F/T range is adjusted in all the four cases. Using maximum values for F_Y, F_Z, T_Y, and T_Z of 60 N, 60 N, 1 Nm, and 1 Nm, respectively, the applied stresses to the entire body of the flexure are kept under the yield strength limits. Also, with these limits the maximum deformations at the normal and shear force sensing cells are set as 0.085 and 0.065 mm, respectively, since the six distances are determined as 0.1 mm depending on general machining technology. Theoretical data computed with the same conditions match the simulation data with over 90% accuracy. As the result, we could expect to change the sensor's F/T range simply by revising the dimensions of the flexure before actual machine production. The process is, therefore, suitable for mass customization.

E. Manufacturing of Six-Axis F/T Sensor

Based on the aforementioned configuration and analyses, the proposed six-axis F/T sensor was manufactured. All the five parts shown in Fig. 8(a) were manufactured via conventional machine works and surface treatment with anodizing was applied to shield electromagnetic noises.
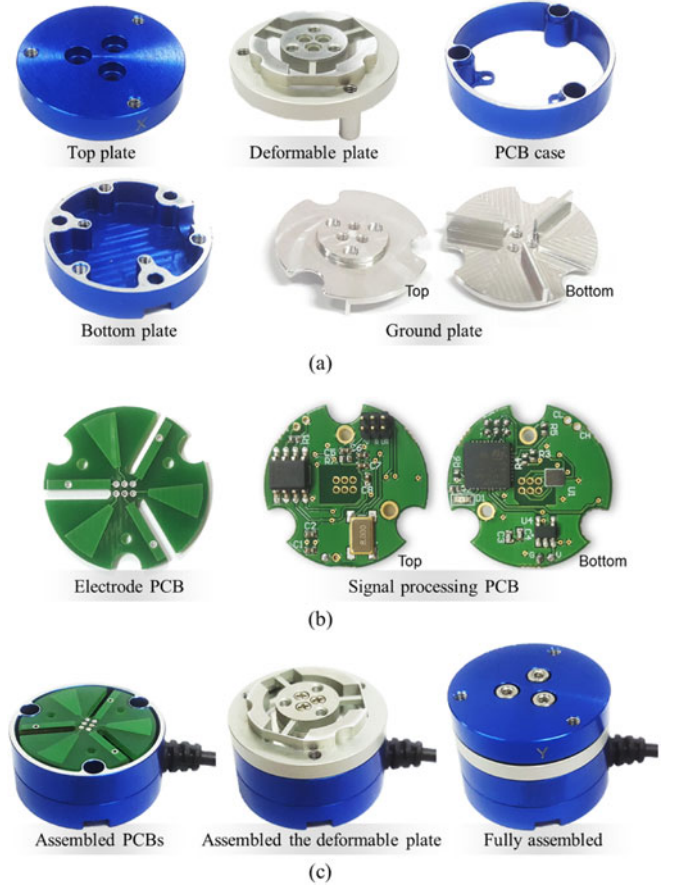

Fig. 8. Manufactured six-axis F/T sensor. (a) Manufactured mechanical parts. (b) Manufactured PCBs. (c) Assembly process of the developed sensor.

As shown in Fig. 8(b), six electrodes of the normal and shear force sensing cells lie on the single PCB. A capacitance-digit-converter (CDC) chip (AD7147, Analog Devices) and a microcontroller (MCU) chip (STM32F103 series, ST) are placed on the signal processing PCB. The digitized capacitance data at the CDC chip are transferred to the MCU chip through an I^2C communication interface. The signal processing PCB sends the digitized data to the computer through a controller area network communication bus.

Fig. 8(c) shows the assembly process of the sensor. After installing the PCBs to the case part, the deformable plate and top plate are plugged into the case part. Once the bolting on the three junctures is done, the assembly process ends. Since all the parts are designed as circular plates, the sensor is simple and compact even after integrating all the electronics.

The sensor's physical dimensions, sampling rate, and force measurement range are summarized in Table I.

IV. EXPERIMENTAL EVALUATIONS

A. Calibration and Transformation of the Six-Axis F/T

As explained above, the shear force can be estimated from the relation $T_Z = F_S a'$. The three shear force sensing cells (Cell$_1$,

Quantity	Value	Unit
Diameter	25	mm
Height	19	mm
Weight	15	g
Force range	± 50	N
Torque range	± 1	Nm

Cell$_3$, and Cell$_5$) are subjected to the same magnitude of shear force measured by the reference sensor (F/T Sensor Nano25, ATI Industrial Automation). Therefore, the relation between measured capacitance data and the shear force measured by the reference sensor can be analyzed. Both the nonlinearity of the measured data and the calibration factor can be found through this relation. The mathematical relation between two datasets was analyzed. Since the variation of the measured capacitances with the applied F/T was approximately exponential, an exponential fit was performed, and thus, the resulting the function is obtained such as

$$f_1(x) = -156.5 + 156.2\exp(-2.91 \cdot 10^{-4}x), \qquad (36)$$

where $f_1(x)$ is the shear force measured by the reference, and x represents the capacitance data. The relation between two datasets were exactly fit by the exponential function. Using this function, the capacitance data becomes linearly calibrated by the shear force by the reference. The calibrated force and reference force match with a one-to-one ratio.

To perform the calibration on the normal force F_N, the relation between the measured capacitance data (C_{Cell4}) and the normal force (F_Z) measured by the reference sensor is analyzed. Again, the relation between variables can be expressed by a fitted exponential function such as

$$f_4(x) = -102.9 + 104.9\exp(-3.12 \cdot 10^{-4}x). \qquad (37)$$

The other cell data (C_{Cell2}, C_{Cell3}, C_{Cell5}, and C_{Cell6}) were analyzed similarly. All the calibrated forces (F_{S1}, F_{S2}, F_{S3}, F_{N1}, F_{N2}, and F_{N3}) were, thus, calculated by using this experimental method.

After obtaining the three normal and three shear forces, a six-axis F/T transformation needs to be obtained. In this section, an automated process is explained to obtain a transformation matrix to map the three normal and three shear forces measured by the sensor to the reference six-axis F/T values. The setup consists of a terminal exposed to the external six-axis F/T, the reference sensor, the developed sensor, and a jig used connecting the top plates of the reference sensor and the developed one as shown in Fig. 9(a) and (b). The six-axis F/T is applied to the terminal, and the F/T is simultaneously measured by two sensors. Because the reference frames ($\{r\}$ and $\{s\}$) of each sensor are placed at the same material point of the sensors' surface, both sensors are exposed to the same magnitude of F/T but the directions are opposite as shown in Fig. 9(a). In this setup, the relationship between the six forces measured by the sensor and the six-axis F/T value
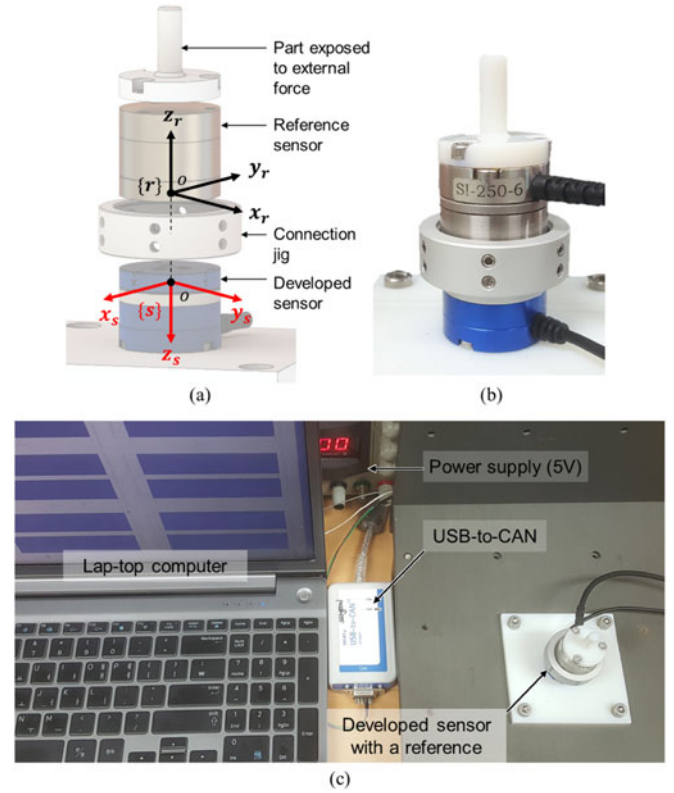

Fig. 9. Experimental setup used to compare the six-axis F/T data measured by the developed sensor with the reference data. (a) Automated transformation setup used to obtain the transformation matrix mapping the measured force data into the six-axis F/T. (b) Assembled state. (c) Experimental environment.

measured by the reference can be written as follows [4], [16]:

$$\mathbf{T} \cdot [F_{S1} \ F_{N1} \ F_{S2} \ F_{N2} \ F_{S3} \ F_{N3}]^T = [F_X \ F_Y \ F_Z T_X \ T_Y \ T_Z]^T \qquad (38)$$

where $\mathbf{T} \in \mathbf{R}^{6 \times 6}$ is a transformation matrix, and $[F_{S1} \ F_{N1} \ F_{S2} \ F_{N2} \ F_{S3} \ F_{N3}]^T$ is the vector of the three normal and three shear forces measured by the developed sensor. $[F_X \ F_Y \ F_Z \ T_X \ T_Y \ T_Z]^T$ is the vector of the six-axis F/T data measured by the reference. Using a linear least-squares method from the correlation of the six-axis F/T with the normal and shear forces according to (38), all the elements of the matrix are automatically computed and the $\mathbf{T}$ is obtained by

$$\mathbf{T} = \begin{bmatrix} -69.9 & 35.3 & 50.1 & -26.3 & -3.1 & -22.7 \\ 11.2 & 27.8 & 13.9 & -20.6 & 21.3 & 8.2 \\ -4.9 & 31.3 & 2.1 & 44.5 & 3.4 & 25.9 \\ 0.02 & 0.31 & 0.03 & -1.32 & 0.01 & 0.63 \\ 0.01 & -0.83 & 0.01 & 0.49 & 0.02 & 0.47 \\ 0.58 & -0.048 & 0.46 & -0.26 & 0.15 & 0.042 \end{bmatrix} \times 10^{-2}.$$
$$\qquad (39)$$

As discussed previously, the F_Z, T_X, and T_Y are derived only by the normal force sensing cells without being influenced from the shear force sensing ones. Therefore, in the $\mathbf{T}$ matrix, elements related to the normal force sensing cells on the third, fourth, and fifth rows are much bigger than the others. On the

TABLE II
SPECIFICATIONS OF THE SENSOR

Quantity	Value	Unit
Resolution of forces	52, 48, 9.5	mN
Resolution of torques	0.9, 1.2, 1.1	mN·m
Relative error of forces	0.75, 0.92, 1.18	% of FSO
Relative error of torques	1.72, 1.86, 0.33	% of FSO
Average hysteresis	1.07	% of FSO
Average repeatability	0.93	% of FSO

*FSO: Full-scale force/torque ranges.

other hand, elements related to the normal force are counted because the shear force sensing cells are affected by T_X and T_Y related to the normal force. Based on this matrix, hysteresis and repeatability of six-axis F/T sensing are evaluated via five repeated measurements. The results are summarized in Table II.

B. Experiments and Discussions

To evaluate the developed sensor, an experimental setup shown in Fig. 9(c) was prepared. It is composed of the reference sensor (F/T Sensor Nano25, ATI Industrial Automation), the developed sensor, jigs for fixing the two sensors, one laptop computer, and a 5 V power supply. The computed calibration equations and the transformation matrix were implemented with the Lab-View software. Using this setup, external forces and torques were randomly applied to the two sensors, and simultaneously measured during 70 s.

The data measured by the developed sensor and the reference one are as shown in Fig. 10(a). Because the shifting phenomena of the F/T are generated by the exponential functions, the data were recorded after offsetting the shifted F/T to zero. Although the six-axis F/T is applied simultaneously, both datasets are very similar for almost all the six-axis F/T data without the intervention among the each six-axis F/T value. The graphs explain that the applied F/T is exposed to F_Z, T_Y, T_X, F_X, F_Y, and T_Z, in order. Here, when F_Z is not exactly applied to the material point, T_X and T_Y are applied to the sensor as displayed from 8 to 16 s of the graphs. Also, when T_X and T_Y are not exactly applied to the axis of rotation, F_Y and F_X are applied as displayed from 18 to 33 s of the graphs. In reverse, during applying F_X and F_Y from 35 to 66 s, T_Y and T_X are applied. Theses phenomena are checked in the six-axis F/T measured by the developed sensor and the reference sensor, simultaneously. Thus, the feasibility of the developed sensor is validated by the well-matched two sensor's data and the phenomena. The errors occurring at each one of the six-axis F/T data were presented in Fig. 10(b) and (c). The mean values of the relative errors of the measured forces are 0.75% , 0.92% , and 1.18%, and the maximum errors are 4.89% , 3.82%, and 4.27%. In the case of the measured torques, the mean values of the relative errors are 1.72% , 1.86%, and 0.33%, and the maximum errors are 5.33% , 7.05%, and 3.68%. Also, resolution was analyzed with 52, 48 and 9.5 mN forces, and 0.9, 1.2, and 1.1 mNm torques, without any error compensation algorithm [24]. The resolutions are summarized in Table II.
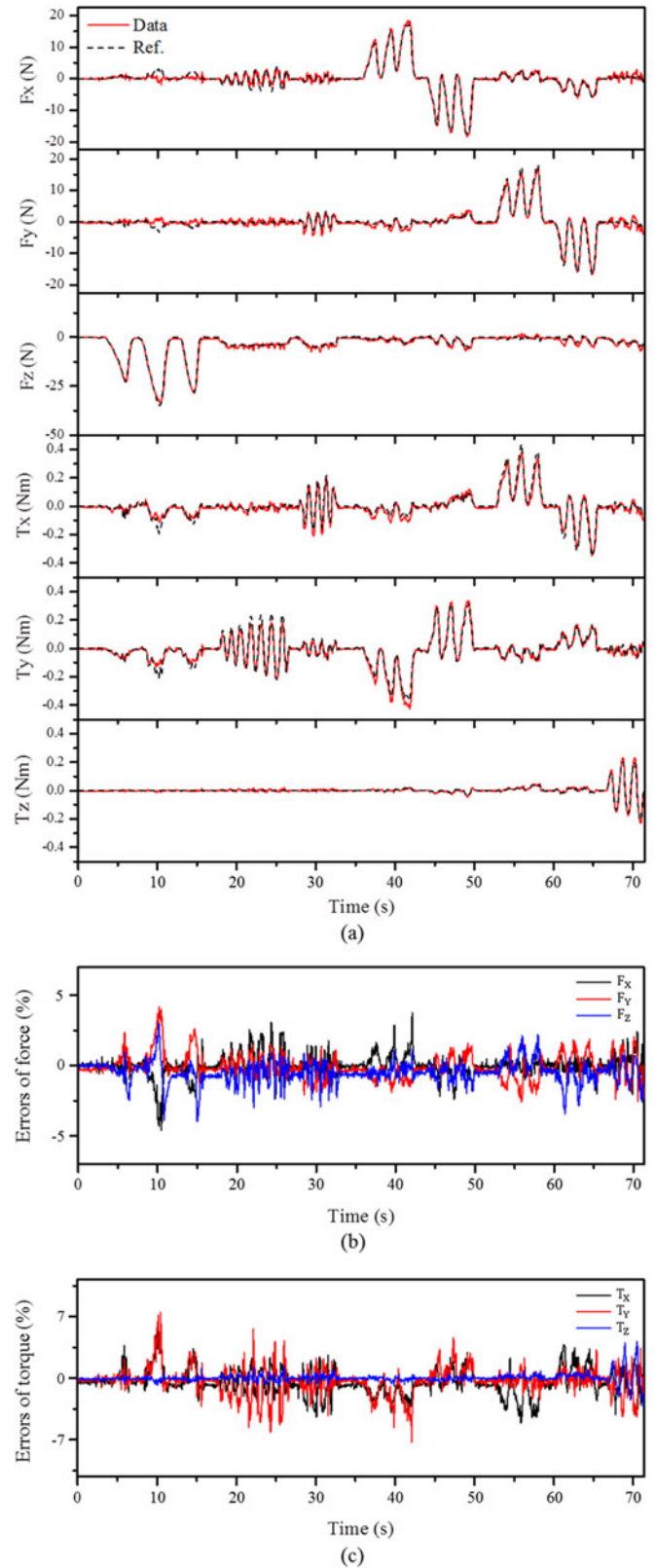

Fig. 10. (a) Time-domain responses of the six-axis F/T measured by the developed sensor (red) and the reference sensor (black dotted). (b) Difference between the measured forces and the reference forces. (c) Difference between the measured torques and the reference torques.

As a result, the proposed sensor is developed to measure a six-axis F/T with about one-twentieth the cost and one-fourth the weight of the reference sensor, integrating all electronics that are essential to the signal processing.

V. Conclusion

In this paper, a novel six-axis F/T sensor based on capacitive transduction principle was presented. The six-axis F/T sensing is performed by six capacitance sensor cells, detecting normal and shear forces. The cells were designed by using both parallel and orthogonal arrangements of the two electrode plates. Shear force sensing was achieved by detecting distance variations between two orthogonal electrodes, not with the universal sensing method of detecting variations in the overlapping area of two electrodes. It provides high sensitivity in six-axis F/T sensing.

The proposed sensor is composed of only five mechanical plate-shaped parts, and two PCBs, and its assembly process requires only several boltings. As the result, the manufacturing and assembly processes are simple, and mass production and customization are possible. This simple configuration allows for very low weight, compactness in size, and cost-effectiveness. Also, since all the electronic components are integrated into the inner part of the sensor, additional devices such as signal amplifiers are not required. The sensor is expected to be used in the future in a wide variety of robotic systems.

References

[1] R. S. Dahiya, G. Metta, M. Valle, and G. Sandini, "Tactile sensingfrom humans to humanoids," *IEEE Trans. Robot.*, vol. 26, no. 1, pp. 1–20, Feb. 2010.

[2] P. Puangmali, K. Althoefer, L. D. Seneviratne, D. Murphy, and P. Dasgupta, "State-of-the-art in force and tactile sensing for minimally invasive surgery," *IEEE Sensor J.*, vol. 8, no. 4, pp. 371–381, Apr. 2008.

[3] M. I. Tiwana, S. J. Redmond, and N. H. Lovell, "A review of tactile sensing technologies with applications in biomedical engineering," *Sensor Actuators A, Phys.*, vol. 179, pp. 17–31, 2012.

[4] U. Kim, D.-H. Lee, W. J. Yoon, B. Hannaford, and H. R. Choi, "Force sensor integrated surgical forceps for minimally invasive robotic surgery," *IEEE Trans. Robot.*, vol. 31, no. 5, pp. 1214–1224, Oct. 2015.

[5] Q. Liang, D. Zhang, Q. Song, Y. Ge, H. Cao, and Y. Ge, "Design and fabrication of a six-dimensional wrist force/torque sensor based on E-type membranes compared to cross beams," *Measurement*, vol. 43, pp. 1702–1719, 2010.

[6] H. Kawasaki, T. Komatsu, and K. Uchiyama, "Dexterous anthropomorphic robot hand with distributed tactile sensor: Gifu hand II," *IEEE/ASME Trans. Mechatronics*, vol. 7, no. 3, pp. 296–303, Sep. 2002.

[7] G.-S. Kim, H.-J. Shin, and J. Yoon, "Development of 6-axis force/moment sensor for a humanoid robot's intelligent foot," *Sensors Actuators A, Phys.*, vol. 141, pp. 276–281, 2008.

[8] R. Ozawa, S. Arimoto, S. Nakamura, and J.-H. Bae, "Control of an object with parallel surfaces by a pair of finger robots without object sensing," *IEEE Trans. Robot.*, vol. 21, no. 5, pp. 965–976, Oct. 2005.

[9] U. Seibold, B. Kubler, and G. Hirzinger, "Prototype of instrument for minimally invasive surgery with 6-axis force sensing capability," in *Proc. IEEE Int. Conf. Robot. Autom.*, 2005, pp. 498–503.

[10] J. J. Craig, *Introduction to Robotics: Mechanics and Control*, 3rd ed. Englewood Cliffs, NJ, USA: Prentice Hall, 2003.

[11] K. Jung *et al.*, "Evaluation of fingertip F/T sensor for dexterous manipulation," in *Proc. IEEE Int. Conf. Ubiquitous Robot. Ambient Intell.*, 2011, pp. 442–445.

[12] S. C. B. Mannsfeld *et al.*, "Highly sensitive flexible pressure sensors with micro-structured rubber as the dielectric layer," *Nature Mater.*, vol. 9, pp. 859–864, 2010.

[13] D.-H. Lee, U. Kim, T. Gulrez, W. J. Yoon, B. Hannaford, and H. R. Choi, "A laparoscopic grasping tool with force sensing capability," *IEEE/ASME Trans. Mechatronics*, vol. 21, no. 1, pp. 130–141, Feb. 2016.

[14] P. Peng and R. Rajamani, "Flexible microtactile sensor for normal and shear elasticity measurements," *IEEE Trans. Ind. Electron.*, vol. 59, no. 12, pp. 4907–4913, Dec. 2012.

[15] D. Kim *et al.*, "Six-axis capacitive force/torque sensor based on dielectric elastomer," in *Proc. Electroactive Polymer Actuators Devices*, 2013, vol. 8687, pp. 1–9.

[16] D.-H. Lee, U. Kim, H. Jung, and H. R. Choi, "A capacitive type novel 6-axis force/torque sensor for robotic applications," *IEEE Sensors J.*, vol. 16, pp. 2290–2299, 2016.

[17] F. P. Sinden and R. A. Boie, "A planar capacitive force sensor with six degrees of freedom," in *Proc. IEEE Int. Conf. Robot. Autom.*, 1986, pp. 1806–1814.

[18] Y. Xiang, "The electrostatic capacitance of an inclined plate capacitor," *J. Electrostatist.*, vol. 64, pp. 29–34, 2006.

[19] Y. Xiang, "Further study on electrostatic capacitance of an inclined plate capacitor," *J. Electrostatist.*, vol. 66, pp. 366–368, 2008.

[20] P. Puangmali, H. Liu, L. D. Seneviratne, P. Dasgupta, and K. Althoefer, "Miniature 3-axis distal force sensor for minimally invasive surgical palpation," *IEEE/ASME Trans. Mechatronics*, vol. 17, no. 4, pp. 646–656, Aug. 2012.

[21] M. I. Tiwanaa, A. Shashankb, S. J. Redmondb, and N. H. Lovell, "Characterization of a capacitive tactile shear sensor for application in robotic and upper limb prostheses," *Sensors Actuators A, Phys.*, vol. 165, pp. 164–172, 2008.

[22] J. Ma and A. Song, "Fast estimation of strains for cross-beams six-axis force/torque sensors by mechanical modeling," *Sensors*, vol. 13, no. 5, pp. 6669–6686, 2013.

[23] S. Timoshenko and J. M. Gere, *Mechanics of Materials*. Monterey, CA, USA: Brooks/Cole, 1972.

[24] M. B. Hong and Y.-H. Jo, "Design and evaluation of 2-DOF compliant forceps with force-sensing capability for minimally invasive robot surgery," *IEEE Trans. Robot.*, vol. 28, no. 4, pp. 932–941, Aug. 2012.

Uikyum Kim received the B.S. degree in mechanical engineering from Sungkyunkwan University, Suwon, South Korea, in 2011, where he is currently working toward the Ph.D. degree in mechanical engineering at the School of Mechanical Engineering, Sungkyunkwan University, Seoul, South Korea.

Since 2011, he has been with Intelligent Robotics and Mechatronic System Laboratory, School of Mechanical Engineering, Sungkyunkwan University. His research interests include surgical robotics, various sensor and actuator systems for robotic applications, haptic interfaces, computing algorithms for automated system, and force-feedback control system.

Dong-Hyuk Lee received the B.S. degree in mechanical engineering, the M.S. degree in mechatronics engineering, and the Ph.D. degree in mechanical engineering from Sungkyunkwan University, Suwon, South Korea, in 2008, 2010, and 2015, respectively.

Since 2015, he has been with Robot Cognition and Control Lab., Korea Institute of Industrial Technology, Ansan, South Korea, where he is a Postdoctoral Researcher. His research interests include medical and industrial robotics, various sensor and actuator systems, and distributed computing for robot applications.

Yong Bum Kim received the B.S. degree in robotics from Ritsumeikan University, Kyoto, Japan, in 2012, where he is currently working toward the Ph.D degree in mechanical engineering at the School of Mechanical Engineering.

Since 2012, he has been with Intelligent Robotics and Mechatronic System Laboratory, School of Mechanical Engineering, Sungkyunkwan University, Suwon, South Korea. His research interests include control of a precision robot hand manipulator, surgical robot, and robot sensing system.

Dong-Yeop Seok received the B.S. degree in mechanical engineering from Sungkyunkwan University, Suwon, South Korea, in 2015, where he is currently working toward the Ph.D. degree in mechanical engineering at the School of Mechanical Engineering. He has been with Intelligent Robotics and Mechatronic System Laboratory, School of Mechanical Engineering, Sungkyunkwan University, since 2015. His research interests include surgical robotics, force-feedback control system, force sensing system, and haptic interfaces.

Hyouk Ryeol Choi (M'95) received the B.S. degree from Seoul National University, Seoul, South Korea, the M.S. degree from the Korea Advanced Institute of Science and Technology, Daejeon, South Korea, and the Ph.D. degree from Pohang University of Science and Technology, Pohang, South Korea, in 1984, 1986, and 1994, respectively, all in mechanical engineering.

From 1986 to 1989, he was an Associate Research Engineer with the IT Research Center, LG Electronics. From 1993 to 1995, he was a Postdoctoral Researcher with Kyoto University, Kyoto, Japan. From 1999 to 2000, he was a JSPS Fellow with the National Institute of Advanced Industrial Science and Technology, Japan. From 2008 to 2009, he was a Visiting Professor with the University of Washington, Seattle, WA, USA. Since 1995, he has been a Full Professor with the School of Mechanical Engineering, Sungkyunkwan University, Suwon, South Korea. His research interests include soft robotics, robotic mechanism, field applications of robots, dextrous robotic hand, and manipulation.

Dr. Choi is an Editor of the *International Journal of Control, Automation and System*, and an Associate Editor of the IEEE/ASME TRANSACTIONS ON MECHATRONICS, and the *Journal of Intelligent Service Robotics*. He serves as a Co-chair of the IEEE RAS technical committee "Robot Hand, Grasping and Manipulation." He was the General Chair of the 2012 IEEE Conference on Automation Science and Engineering, Seoul, South Korea.